Off-Diagonal Majorana Vector Currents, Exact Six-Gamma Trace Algebra & Coupled-Channel Yukawa Limit

Shide Feng and Jingxu Wu*
Faculty of Physics, Lomonosov Moscow State University
Moscow 119991, Russia • wuxj@my.msu.ru

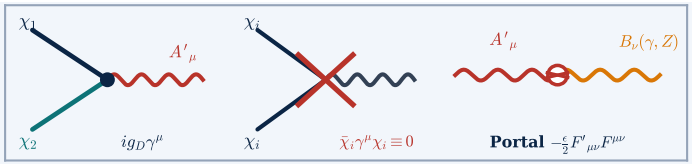
1. Pseudo-Dirac Dark Sector & $U(1)'$ Gauge Portal

In a CP-conserving realization of threshold-excited dark matter, two opposite-charge Weyl spinors (ξ, η) couple to a broken $U(1)'$ gauge boson A'_μ ($g_D \equiv \sqrt{4\pi\alpha_D}$) with Dirac mass m_D and Majorana mass $0 < m_M \ll m_D$:

$$\mathcal{L}_{\rm mass} = -\frac{1}{2}\begin{pmatrix}\xi & \eta\end{pmatrix}\begin{pmatrix} m_M & m_D \\ m_D & m_M\end{pmatrix}\begin{pmatrix}\xi \\ \eta\end{pmatrix} + \text{h.c.}, \qquad \begin{aligned} m_{1,2} &= m_D \mp m_M, \\ \delta &\equiv m_2 - m_1 = 2m_M. \end{aligned}$$

Takagi rephasing ($\theta_W = \pi/4$) yields two self-conjugate Majorana mass eigenstates χ_1, χ_2. Because Majorana diagonal vector currents vanish identically ($\bar\chi_i\gamma^\mu\chi_i = 0$), the transition vector current is purely off-diagonal:

$$\mathcal{L}_{\rm int} = ig_D A'_\mu \bar\chi_2\gamma^\mu\chi_1 - \frac{\epsilon}{2}F'_{\mu\nu}F^{\mu\nu}, \qquad (\bar\chi_2\gamma^\mu\chi_1)^\dagger = -\bar\chi_2\gamma^\mu\chi_1.$$



For $\chi_1(p_1)\chi_1(p_2) \to \chi_2(k_1)\chi_2(k_2)$ in the center-of-mass (CM) frame with per-particle energy $E = m_1/\sqrt{1 - v_{\rm rel}^2/4}$, initial momentum $k_i = \sqrt{E^2 - m_1^2}$, final momentum $k_f = \sqrt{E^2 - m_2^2}$, and relative speed $v_{\rm rel} = 2k_i/E$, the exact threshold is:

$$v_{\rm th} \equiv \frac{2\sqrt{m_2^2 - m_1^2}}{m_2} \simeq \sqrt{\frac{8\delta}{m_1}}, \qquad k_f^2 = \frac{m_2^2}{4 - v_{\rm rel}^2}\left(v_{\rm rel}^2 - v_{\rm th}^2\right) \propto \Delta_v \equiv \frac{v_{\rm rel}^2 - v_{\rm th}^2}{v_{\rm th}^2}.$$

2. Relativistic Trace Algebra & Closed-Form $\sigma(v_{\rm rel})$

Identical final-state Majorana fermions require the antisymmetrized amplitude $\mathcal{M} = \mathcal{M}_t - \mathcal{M}_u$ with Mandelstam invariants $s = 4E^2$ and $t, u - m_{A'}^2 = -(A \mp Bc)$ ($c \equiv \cos\theta$, $A \equiv k_i^2 + k_f^2 + m_{A'}^2$, $B \equiv 2k_ik_f$):

$$\frac{d\sigma}{d\Omega} = \frac{g_D^4}{512\pi^2 s}\frac{k_f}{k_i}\left[\frac{T_{tt}(c)}{(A - Bc)^2} + \frac{T_{tt}(-c)}{(A + Bc)^2} - \frac{2T_{tu}}{A^2 - B^2c^2}\right].$$

Using $\mathrm{Tr}[\gamma_\mu\not{a}\gamma_\nu\not{b}]\,\mathrm{Tr}[\gamma^\mu\not{c}\gamma^\nu\not{d}] = 32[(a\cdot c)(b\cdot d) + (a\cdot d)(b\cdot c)]$, the direct trace T_{tt} and single 6-gamma crossed trace $T_{tu} = \mathrm{Tr}[\gamma^\mu(\not{p}_1 + m_1)\gamma^\nu(\not{k}_2 + m_2)\gamma_\mu(\not{p}_2 + m_1)\gamma_\nu(\not{k}_1 + m_2)]$ evaluate in closed form to:

$$\begin{aligned} T_{tt} &= 32(k_1\cdot k_2)(p_1\cdot p_2) + 32(k_1\cdot p_2)(p_1\cdot k_2) - 32m_1m_2(k_1\cdot p_1 + k_2\cdot p_2) + 64m_1^2m_2^2 \\ &= T_0 + T_1c + T_2c^2, \qquad T_1 = 64k_ik_f(E^2 + m_1m_2), \quad T_2 = 32k_i^2k_f^2, \\ T_{tu} &= -128E^4 + 96E^2(m_1^2 + m_2^2) + 64E^2m_1m_2 - 96m_1^2m_2^2 \quad \text{(independent of } \theta!). \end{aligned}$$

Defining the elementary rational angular integrals over $c \in [-1, 1]$:

$$J_0 = \frac{2}{A^2 - B^2}, \quad J_1 = \frac{2A}{B(A^2 - B^2)} - \frac{1}{B^2}\ln\frac{A+B}{A-B}, \quad J_2 = \frac{2A^2}{B^2(A^2 - B^2)} - \frac{2A}{B^3}\ln\frac{A+B}{A-B} + \frac{2}{B^2},$$

and $K_0 = \frac{1}{AB}\ln\frac{A+B}{A-B}$, the exact total cross section and its $k_f \to 0$ threshold expansion ($J_0, K_0 \to 2/A^2$, $J_1 = \mathcal{O}(k_f)$, $T_1J_1 = \mathcal{O}(k_f^2)$) are:

$$\sigma(v_{\rm rel}) = \frac{g_D^4}{128\pi s}\frac{k_f}{k_i}\left[T_0J_0 + T_1J_1 + T_2J_2 - T_{tu}K_0\right] \underset{\Delta_v \ll 1}{=} \frac{g_D^4(T_0 - T_{tu})}{64\pi s k_i A^2}k_f\left[1 + \mathcal{O}(k_f^2)\right].$$

3. Static Yukawa Born Limit & Coupled-Channel System

In the nonrelativistic heavy-mediator limit ($B \ll A$), averaging singlet $(1/4, |\widetilde V(q) + \widetilde V(q')|^2)$ and triplet $(3/4, |\widetilde V(q) - \widetilde V(q')|^2)$ exchange weights for $\widetilde V(q) = -4\pi\alpha_D/(q^2 + m_{A'}^2)$ gives the potential Born cross section:

$$\sigma^{\rm pot}(v_{\rm rel}) = \frac{k_f}{k_i}\mu_1\mu_2\alpha_D^2\left[\frac{16\pi}{A^2 - B^2} - \frac{4\pi}{AB}\ln\frac{A+B}{A-B}\right] \underset{B\ll A}{\longrightarrow} \frac{8\pi\mu_1\mu_2\alpha_D^2}{m_{A'}^4}\frac{k_f}{k_i}.$$

Outside the perturbative Born regime ($\eta \equiv \alpha_D\mu_1/m_{A'} \ll 1$), multi-$A'$ exchange obeys the two-channel radial Schrödinger system ($\mu_i = m_i/2$, $\epsilon = \mu_1 v_{\rm rel}^2/2$):

$$\left[-\frac{1}{2\mu_i}\frac{d^2}{dr^2} + \frac{\ell(\ell+1)}{2\mu_i r^2} + 2\delta\,\delta_{i2} - \epsilon\right]u_i(r) = \frac{\alpha_D e^{-m_{A'}r}}{r}u_{3-i}(r), \quad S_{\rm cc} \equiv \frac{\sigma_{\rm Sch}}{2\sigma_{\rm Born}^{\rm QFT}}.$$

$v_{\rm rel}/v_{\rm th}$	k_f/m_1	Closed σ (2.47)	Quadr. (2.42)	Potential $\sigma^{\rm pot}$	$\sigma/\sigma^{\rm pot}$
1.01	5.671×10^{-5}	1.08886×10^{-8}	1.08886×10^{-8}	1.08886×10^{-8}	1.000000
1.10	1.833×10^{-4}	3.23156×10^{-8}	3.23156×10^{-8}	3.23156×10^{-8}	1.000000
2.00	6.928×10^{-4}	6.71779×10^{-8}	6.71779×10^{-8}	6.71778×10^{-8}	1.000002
5.00	1.960×10^{-3}	7.60037×10^{-8}	7.60037×10^{-8}	7.60028×10^{-8}	1.000012
15.0	5.987×10^{-3}	7.74047×10^{-8}	7.74047×10^{-8}	7.73964×10^{-8}	1.000108

Catastrophic Cancellation Guard: For $B/A \lesssim 10^{-3}$ (at $v_{\rm rel} = 2v_{\rm th}$, $B/A = 1.2\times10^{-7}$), individual terms in J_1, J_2 exceed their net difference by 10^{14} and are evaluated in 60-digit precision (verified against 160-node Gauss–Legendre quadrature to 1.0×10^{-15}).

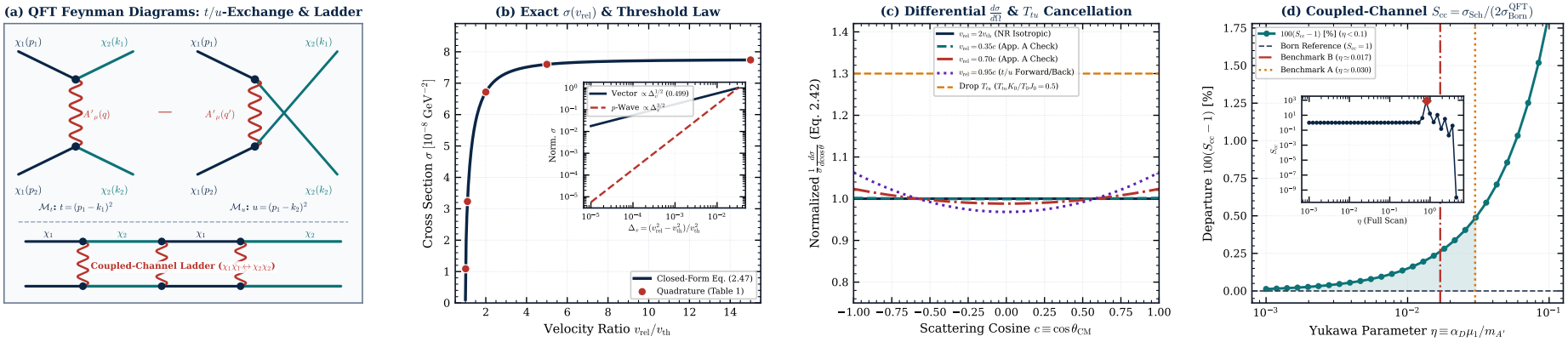


Figure 1 (Microscopic Majorana Kernel & Non-Perturbative Benchmark): **(a)** Tree-level Majorana t- and u-channel Feynman diagrams ($\mathcal{M} = \mathcal{M}_t - \mathcal{M}_u$, no particle-number arrows) and coupled-channel A'_μ ladder ($\chi_1\chi_1 \leftrightarrow \chi_2\chi_2$). **(b)** Closed-form QFT cross section Eq. (2.47) vs. angular quadrature at Benchmark B ($m_1 = 100$ GeV, $m_{A'} = 3m_1$, $v_{\rm th} = 8\times10^{-4}$, $\alpha_D = 0.1$) and $\Delta_v^{1/2}$ threshold power law (fitted exponent 0.499). **(c)** Normalized angular distribution $\frac{1}{\sigma}\frac{d\sigma}{d\cos\theta}$ across relativistic test points. **(d)** Coupled-channel Schrödinger ratio $S_{\rm cc}(\eta)$ (Eq. 2.56) showing $< 0.5\%$ departure at Benchmarks A ($\eta = 0.03$) and B ($\eta = 0.017$).

XXXVIII IWHEPFT Synthesis: Exact angle-independence of the 6-gamma Majorana trace T_{tu} yields a closed-form cross section obeying the exact $\sigma \propto \Delta_v^{1/2}$ half-power threshold law and matching the spin-weighted Yukawa Born limit to 10^{-6}.

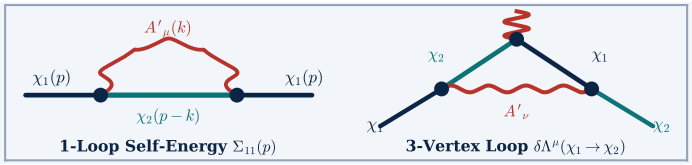
Three-Body Portal Metastability, Microscopic Reciprocity, Milky Way Potential & Pair-Averaged Rates

Shide Feng and Jingxu Wu*
Faculty of Physics, Lomonosov Moscow State University
Moscow 119991, Russia • wuxj@my.msu.ru

1. Excited-State Lifetime & Chemical Reaction Network

For $\delta < m_{A'}$, on-shell A' emission is forbidden. Three-body decay $\chi_2 \to \chi_1 f\bar{f}$ via kinetic mixing $-\frac{\epsilon}{2}F'_{\mu\nu}F^{\mu\nu}$ requires $\delta > 2m_f$; away from threshold its contact-limit width scales as $\Gamma(\chi_2 \to \chi_1 e^+e^-) \propto \epsilon^2\alpha_D\alpha_{\rm em}\delta^5/m^4_{A'}$ (a vector-mediated 3-body transition, not a magnetic dipole decay). Below $2m_e = 1.022$ MeV, all tree-level charged-lepton modes close, naturally motivating the stationary decay-free benchmark:

$$\Gamma_{\rm dec}\, t_{\rm age} \ll 1, \qquad \Gamma_{\rm dec} \ll \Omega_r \qquad \text{(Stationary Decay-Free Regime).}$$



For number densities n_1, n_2 sharing a local velocity distribution, the collisional reaction network for excitation ($k_u = \langle\sigma_u v\rangle$), de-excitation ($k_d = \langle\sigma_d v\rangle$), coannihilation ($k_a = \langle\sigma_a v\rangle$), and decay ($\Gamma_d$) is:

$$\dot{n}_2\Big|_{\rm coll} = n_1^2 k_u - n_2^2 k_d - n_1 n_2 k_a - \Gamma_d n_2,$$
$$\dot{n}_1\Big|_{\rm coll} = -n_1^2 k_u + n_2^2 k_d - n_1 n_2 k_a + \Gamma_d n_2, \qquad \dot{n}_{\rm tot} = -2n_1 n_2 k_a.$$

Here the 1/2! identical-pair factor in the event rate cancels the 2 particles converted per $\chi_1\chi_1 \leftrightarrow \chi_2\chi_2$ event.

2. Chemical Balance Root & Microscopic Reciprocity

In a slowly depleted bath ($n \simeq \rho(r)/m_1$, excited fraction $x_2 \equiv n_2/n \in [0,1]$) with per-particle rates $U(r) = nk_u$, $D(r) = nk_d$, and $A(r) = nk_a$, the fixed-bath chemical balance function is:

$$F(x,r) = U(r)(1-x)^2 - D(r)x^2 - A(r)x(1-x) - \Gamma_d x, \qquad F(x_{2,\rm eq}, r) = 0.$$

Linearizing around the stable local-equilibrium root $0 \le x_{2,\rm eq}(r) \le 1$ defines the positive chemical relaxation rate $\Gamma_{\rm chem}(r) = -\partial_x F|_{x_{2,\rm eq}} > 0$:

$$\Gamma_{\rm chem}(r) = 2U(1-x_{2,\rm eq}) + 2Dx_{2,\rm eq} + A(1-2x_{2,\rm eq}) + \Gamma_d \underset{A=\Gamma_d=0}{=} 2\sqrt{U(r)D(r)}.$$

The pair-averaged radial rates integrate the isotropic speed distribution $p_r(v) = \frac{4\pi v^2}{\rho(r)} f_{\rm Edd}(\Psi - v^2/2)$ up to the maximum relative speed $w_{\max} = 2v_{\rm esc}(r)$:

$$k_{u,d}(r) = \frac{1}{2}\int_0^{v_{\rm esc}(r)} dv_1\, p_r(v_1) \int_0^{v_{\rm esc}(r)} dv_2\, p_r(v_2) \int_{-1}^{1} d\mu\, K_{u,d}\left(\sqrt{v_1^2+v_2^2-2v_1v_2\mu}\right).$$

Exact Microscopic Reciprocity: Detailed balance relates up- and down-scattering cross sections at the same CM energy $\sqrt{s}$ without imposing a thermal Maxwell–Boltzmann ratio on the nonthermal Eddington DF:

$$g_1^2 p_1^2\, \sigma_{11\to22}(s) = g_2^2 p_2^2\, \sigma_{22\to11}(s) \implies \begin{aligned} K_u(w) &= C\sqrt{w^2 - v_{\rm th}^2}\,\Theta(w - v_{\rm th}), \\ K_d(w) &= C\sqrt{w^2 + v_{\rm th}^2}. \end{aligned}$$

3. Three-Component Milky Way Control Potential

To ensure dynamical self-consistency, both the Eddington DF $f_{\rm Edd}(\mathcal{E})$ and the bound halo orbits are defined in the same 3-component spherical Galactic potential $\Phi(r) = \Phi_b(r) + \Phi_{d,\rm sph}(r) + \Phi_h(r)$:

$$\Phi_b(r) = -\frac{GM_b}{r+r_b}, \quad \Phi_{d,\rm sph}(r) = -\frac{GM_d}{\sqrt{r^2+(a+b)^2}}, \quad \Phi_h(r) = -4\pi G\rho_s r_s^3 \frac{\ln(1+r/r_s)}{r}.$$

Galactic Component / Diagnostic	Parameter Specification	Physical Role in Transport
NFW Dark Halo $\Phi_h(r)$	$r_s = 20$ kpc, $\rho_s = 6.668\times10^6 M_\odot$ kpc^{-3}	Tracer density $\rho(r)$ & outer $\Psi(r)$
Hernquist Bulge $\Phi_b(r)$	$M_b = 1.5\times10^{10} M_\odot$, $r_b = 0.6$ kpc	Deepens inner $\Psi(r)$, boosts $2v_{\rm esc}$
Spherical Disk $\Phi_{d,\rm sph}(r)$	$M_d = 6.0\times10^{10} M_\odot$, $a+b = 6.76$ kpc	Equatorial Miyamoto–Nagai surrogate
Solar Circle Kinematics	$R_0 = 8$ kpc, $v_c = 199.11$ km s^{-1}	Local circular speed calibration
Solar Escape Speed	$v_{\rm esc}(8\ {\rm kpc}) = 553.89$ km s^{-1}	Sets threshold scale $x \equiv v_{\rm th}/v_{\rm esc}(R_0)$
Reference Orbit (8 kpc)	$E = E_c(8\ {\rm kpc})$, $L = 0.5L_c$	$\Omega_r^{\rm ref} = 37.9569$ (kpc/km s^{-1})$^{-1}$

Exact Angular Average of Threshold Kernels: In Eq. (4.6), the angular integral $\int_{-1}^{1} d\mu \sqrt{v_1^2+v_2^2-2v_1v_2\mu \mp v_{\rm th}^2}$ is evaluated analytically in closed form on a 72-node speed grid across 220 logarithmic radii (10^{-5}–10^6 kpc), eliminating threshold-cusp quadrature noise. When $v_{\rm th} \ge 2v_{\rm esc}(r)$, $U(r) = 0$ identically while the nonlinear equation retains $-D(r)x_2^2$.

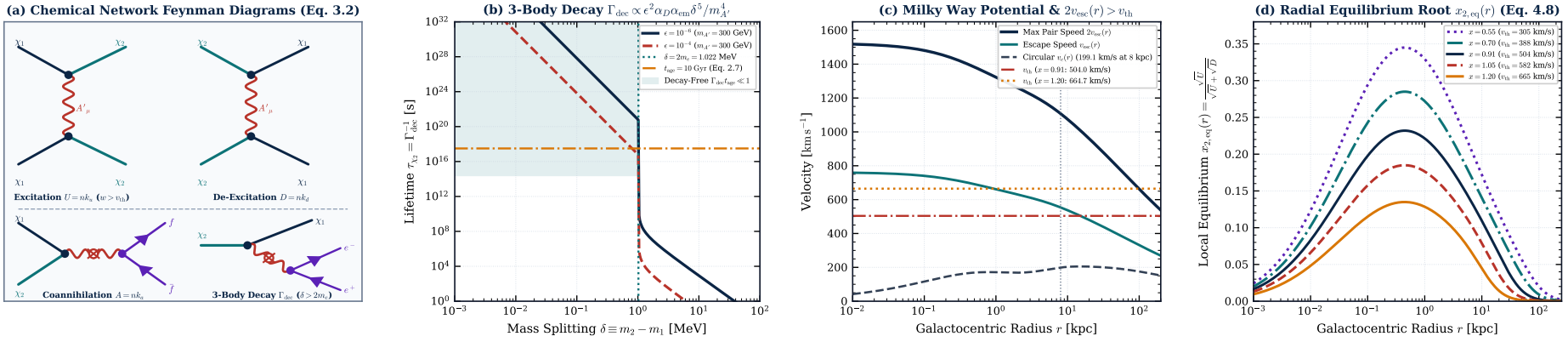


Figure 2 (Chemical Reaction Network, Metastability & Galactic Background): **(a)** Feynman diagrams for the four reaction channels in Eq. (3.2): endothermic excitation $U = nk_u$, exothermic de-excitation $D = nk_d$, passive coannihilation $A = nk_a$, and 3-body portal decay $\Gamma_{\rm dec}$. **(b)** Excited-state lifetime $\tau_{\chi_2}(\delta)$ demonstrating the $\delta < 2m_e$ decay-free halo regime ($\Gamma_{\rm dec}t_{\rm age} \ll 1$). **(c)** Milky Way 3-component potential velocities $2v_{\rm esc}(r), v_{\rm esc}(r), v_c(r)$ vs. threshold $v_{\rm th}$. **(d)** Local chemical equilibrium profile $x_{2,\rm eq}(r) = \sqrt{U}/(\sqrt{U}+\sqrt{D})$ across thresholds $x \in [0.55, 1.20]$.

XXXVIII IWHEPFT Synthesis: Microscopic reciprocity fixes the nonthermal de-excitation kernel $K_d(w)$ without Boltzmann approximations, while the baryon-deepened Milky Way potential governs where $2v_{\rm esc}(r) > v_{\rm th}$ supports pair excitation.

Characteristic Survival Weighting, Action–Angle Transfer Response, Eddington Inversion & Parseval Theorem

Shide Feng and Jingxu Wu*
Faculty of Physics, Lomonosov Moscow State University
Moscow 119991, Russia • wuxj@my.msu.ru

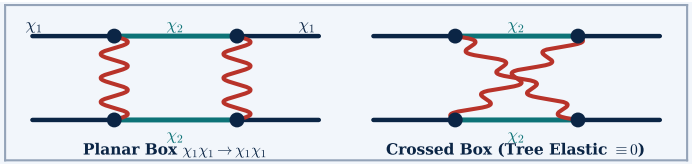
1. Characteristic Green Function & Frozen Asymptotics

Along a bound halo trajectory ending at $(\mathbf{x}, \mathbf{v})$ at time t, the departure $\delta x_2 \equiv x_2 - x_{2,\mathrm{eq}}$ under the linear relaxation closure $\frac{Dx_2}{Dt} = \Gamma_{\mathrm{chem}}(r)[x_{2,\mathrm{eq}}(r) - x_2]$ is governed by the survival weight $W(t,t') = \exp[-\int_{t'}^{t} \Gamma_{\mathrm{chem}}(s)\,ds]$:

$$\delta x_2(t) = W(t,t_0)\,\delta x_2(t_0) - \int_{t_0}^{t} dt'\, W(t,t')\,\dot{x}_{2,\mathrm{eq}}(t'), \qquad \tau_r \equiv \int_0^{T_r} \Gamma_{\mathrm{chem}}(t')\,dt'.$$

For a periodic orbit of radial period $T_r = 2\int_{r_p}^{r_a} dr/|v_r| = 4(r_a - r_p)\int_0^{\pi/2} \frac{\sin\chi\cos\chi}{|v_r(r(\chi))|}\,d\chi$, the unique stationary periodic solution is:

$$x_2^{\mathrm{ss}}(t) = \frac{\int_{t-T_r}^{t} dt'\, W(t,t')\,\Gamma_{\mathrm{chem}}(t')\,x_{2,\mathrm{eq}}(t')}{1 - \exp(-\tau_r)} \quad \Big(\text{evaluated via } -\mathrm{expm1}(-\tau_r)\Big).$$



Distinct Frozen-Chemistry Limits ($\epsilon \to 0$): Scaling $\Gamma_{\mathrm{chem}} = \epsilon g(t)$ in Eq. (3.12) vs. scaling $U = \epsilon u(t)$, $D = \epsilon d(t)$ in the nonlinear pair equation $\dot{x}_2 = U(1-x_2)^2 - Dx_2^2$ yields two distinct orbit-constant asymptotes:

$$x_{2,\mathrm{frozen}}^{\mathrm{linear}} = \frac{\langle g\,x_{2,\mathrm{eq}}\rangle_t}{\langle g\rangle_t} \neq x_{2,\mathrm{frozen}}^{\mathrm{nonlinear}} = \frac{\sqrt{\langle u\rangle_t}}{\sqrt{\langle u\rangle_t} + \sqrt{\langle d\rangle_t}} \quad \text{(neither sets } \Delta_J = -1\text{)}.$$

2. Action–Angle Response & Exact Nonlinear Riccati Map

In a spherical integrable potential with radial action $J_r = \frac{1}{\pi}\int_{r_p}^{r_a} dr\sqrt{2[E-\Phi(r)] - L^2/r^2}$ and angle $\dot{\boldsymbol{\theta}} = \boldsymbol{\Omega}(\mathbf{J})$, expanding $x_{2,\mathrm{eq}} = \sum_{\mathbf{n}} X_{\mathbf{n}}^{\mathrm{eq}} e^{i\mathbf{n}\cdot\boldsymbol{\theta}}$ at orbit-constant rate Γ_{chem} ($\mathrm{Da}_{\mathrm{orb}} \equiv \Gamma_{\mathrm{chem}}/\Omega_r$) gives:

$$X_{\mathbf{n}} = \mathcal{T}_{\mathbf{n}} X_{\mathbf{n}}^{\mathrm{eq}}, \qquad \mathcal{T}_{\mathbf{n}} = \frac{\Gamma_{\mathrm{chem}}}{\Gamma_{\mathrm{chem}} + i\mathbf{n}\cdot\boldsymbol{\Omega}}, \qquad |\mathcal{T}_{\mathbf{n}}| = \frac{\Gamma_{\mathrm{chem}}}{\sqrt{\Gamma_{\mathrm{chem}}^2 + (\mathbf{n}\cdot\boldsymbol{\Omega})^2}}, \quad \phi_{\mathbf{n}} = \arctan\frac{\mathbf{n}\cdot\boldsymbol{\Omega}}{\Gamma_{\mathrm{chem}}}.$$

For the full radially varying nonlinear pair equation ($A = \Gamma_d = 0$), transforming to $q \equiv x_2/(1-x_2)$ yields the Riccati ODE $\dot{q} = U(t) - D(t)q^2$. Parameterizing the orbit by $r(\theta) = \frac{r_a+r_p}{2} - \frac{r_a-r_p}{2}\cos(\theta/2)$ ($0 \le \theta < 2\pi$, $\Delta t_j = \frac{r_a-r_p}{2|v_r|}|\sin\theta_j|\Delta\theta$), each segment is the exact positive fractional-linear map:

$$q_{j+1} = \frac{q_j + b_j}{c_j q_j + 1}, \qquad b_j = U_j h_j, \quad c_j = D_j h_j, \quad h_j = \frac{\tanh\Big(\sqrt{U_j D_j}\,\Delta t_j\Big)}{\sqrt{U_j D_j}}.$$

Multiplying the 2×2 segment matrices $\prod_{j=1}^{N_\theta}\begin{pmatrix} 1 & b_j \\ c_j & 1\end{pmatrix}$ and solving their non-negative eigenvector imposes exact periodicity on both radial branches $x_2^{\pm}(r;\mathcal{E},L) = x_2(r,\pm|v_r|,v_t)$ without integrating thousands of slow cycles.

Parseval's Identity & Single-Orbit Diagnostic: By Parseval's theorem, the equal-time orbit average $\langle x_2(1-x_2)\rangle_t = X_0 - X_0^2 - \sum_{n\neq 0}|\mathcal{T}_n|^2|X_n^{\mathrm{eq}}|^2$ gives a strictly non-negative chemical diagnostic:

$$\mathcal{D}_{\mathrm{orb}} \equiv \frac{\langle x_2(1-x_2)\rangle_t - \langle x_{2,\mathrm{eq}}(1-x_{2,\mathrm{eq}})\rangle_t}{\langle x_{2,\mathrm{eq}}(1-x_{2,\mathrm{eq}})\rangle_t} = \frac{\sum_{n\neq 0}(1-|\mathcal{T}_n|^2)|X_n^{\mathrm{eq}}|^2}{X_0 - X_0^2 - \sum_{n\neq 0}|X_n^{\mathrm{eq}}|^2} \ge 0.$$

3. Regularized Eddington Inversion & Two-Branch Measure

With relative potential $\Psi(r) = -\Phi(r)$ and relative binding energy $\mathcal{E} = \Psi(r) - \frac{1}{2}v^2$, Abel inversion of $\rho(\Psi)$ using analytic radial derivatives $\frac{d^2\rho}{d\Psi^2} = \frac{\rho''\Psi' - \rho'\Psi''}{(\Psi')^3}$ and $\Psi = \mathcal{E}(1-t^2)$ gives the nonsingular Eddington DF:

$$f_{\mathrm{Edd}}(\mathcal{E}) = \frac{1}{\sqrt{8}\pi^2}\left[\int_0^{\mathcal{E}} \frac{d\Psi}{\sqrt{\mathcal{E}-\Psi}}\frac{d^2\rho}{d\Psi^2} + \frac{1}{\sqrt{\mathcal{E}}}\left(\frac{d\rho}{d\Psi}\right)_{\Psi=0}\right] = \frac{2\sqrt{\mathcal{E}}}{\sqrt{8}\pi^2}\int_0^1 dt\,\frac{d^2\rho}{d\Psi^2}\Big|_{\Psi=\mathcal{E}(1-t^2)}.$$

Changing variables at fixed radius r from (v_r, v_t) to $(\mathcal{E}, L)$ introduces the exact phase-space measure $v_t dv_t|dv_r| = \frac{L\,dL\,d\mathcal{E}}{r^2|v_r|}$ across both radial branches. Mapping to local quadrature coordinates $u = v/v_{\mathrm{esc}}(r) \in [0,1]$ and $\mu = |v_r|/v \in [0,1]$ ($\mathcal{E} = \Psi(1-u^2)$, $L = rv_{\mathrm{esc}}u\sqrt{1-\mu^2}$) removes the $|v_r|^{-1}$ turning-point singularity:

$$\bar{x}_2(r) \equiv \frac{m_1 n_2(r)}{\rho(r)} = \frac{4\pi v_{\mathrm{esc}}^3(r)}{\rho(r)}\int_0^1 du\,u^2 f_{\mathrm{Edd}}\Big[\Psi(r)(1-u^2)\Big]\int_0^1 d\mu\,\frac{x_2^+(r;\mathcal{E},L) + x_2^-(r;\mathcal{E},L)}{2}.$$

Rate $y = \Gamma_{\mathrm{chem}}(8\ \mathrm{kpc})/\Omega_r^{\mathrm{ref}}$	Linear, All-Sky	Nonlinear, All-Sky	Nonlinear, 1°–10°	Regime ($x = 0.91$)
$y = 0.01$	−0.7144%	−1.0484%	−1.3312%	Slow / Frozen Memory
$y = 0.10$	−0.7240%	−1.0545%	−1.2674%	Intermediate-Slow
$y = 1.00$	−0.7127%	−0.9178%	−0.2780%	Orbital Resonance
$y = 16.0$	−0.0213%	−0.0285%	−0.0017%	Fast Relaxation
$y = 100$	−0.0007%	−0.0012%	−0.0002%	Local Equilibrium

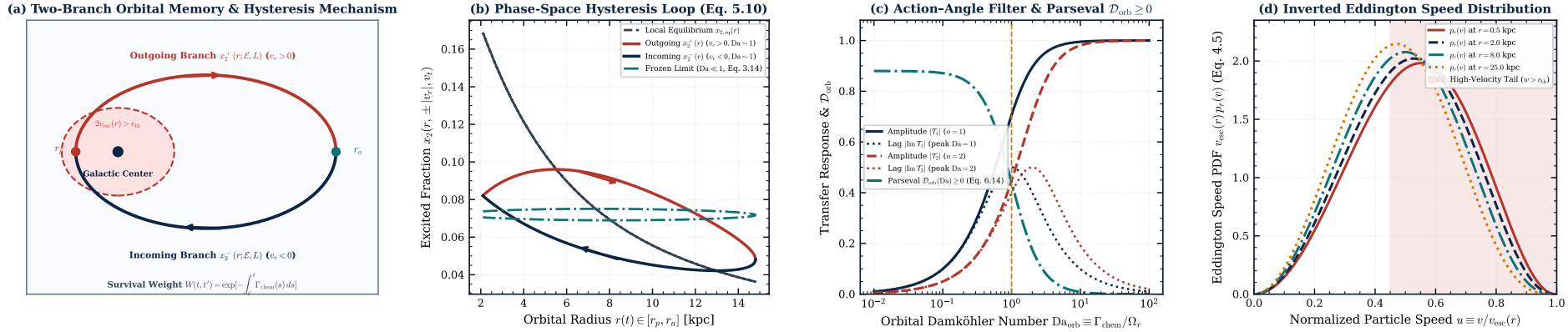


Figure 3 (Orbital Transport Hysteresis, Action–Angle Filtering & Eddington Reconstruction): **(a)** Phase-space mechanism of two-branch orbital memory: particles excited inside the inner high-velocity zone ($2v_{\mathrm{esc}} > v_{\mathrm{th}}$) carry excess χ_2 outward along $x_2^+(r)$ ($v_r > 0$) while incoming $x_2^-(r)$ ($v_r < 0$) retains outer-halo depletion. **(b)** Exact hysteresis loop $x_2^+(r)$ vs. $x_2^-(r)$ along an eccentric bound orbit ($r_p = 2.1$ kpc, $r_a = 14.8$ kpc). **(c)** Action–angle amplitude $|\mathcal{T}_n|$, lag $|\mathrm{Im}\,\mathcal{T}_n|$, and non-negative Parseval diagnostic $\mathcal{D}_{\mathrm{orb}} \ge 0$ (Eq. 6.14). **(d)** Regularized Eddington speed distribution $p_r(v)$ across galactocentric radii.

XXXVIII IWHEPFT Synthesis: Because $n_1(r)$ and $n_2(r)$ are reconstructed over (u,μ) before forming $q(r) = n_1 n_2$, spatial DF weighting converts $\mathcal{D}_{\mathrm{orb}} \ge 0$ into a net all-sky suppression ($\Delta_J(4\pi) = -1.05\%$ at $x = 0.91, y = 0.01$).

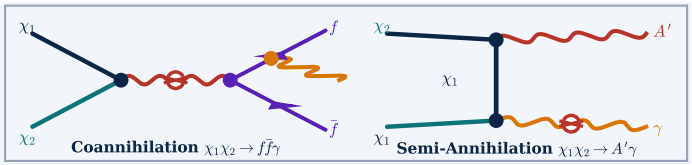
Coannihilation Emissivity Factoring, 6×6 Nonlocal J-Factor Grid, Brightness Ratio $R(\psi)$ & 10 Gyr Memory

Shide Feng and Jingxu Wu*
Faculty of Physics, Lomonosov Moscow State University
Moscow 119991, Russia • wuxj@my.msu.ru

1. Coannihilation Emissivity & Aperture Identity

For a passive, velocity-independent coannihilation tracer ($k_a = \text{const}$), the spatial number densities $n_1(r) = \frac{\rho(r)}{m_1} - n_2(r)$ and $n_2(r)$ are integrated separately over phase space before forming the emissivity $q(r)$:

$$q(r) = n_1(r)n_2(r) = \frac{\rho^2(r)}{m_1^2}\bar{x}_2(r)\Big[1-\bar{x}_2(r)\Big], \qquad \langle x_2(1-x_2)\rangle_v \neq \langle x_2\rangle_v\Big[1-\langle x_2\rangle_v\Big].$$



For an observer at $\mathbf{x}_\odot = (R_0, 0, 0)$ ($R_0 = 8$ kpc) viewing direction $\hat{\mathbf{n}} = (-\cos b\cos l, \cos b\sin l, \sin b)$ at angle $\cos\psi = \cos b\cos l$ ($0 \le \ell \le 250$ kpc, $r(\ell,\psi) = \sqrt{R_0^2 + \ell^2 - 2R_0\ell\cos\psi}$), the directional intensity and aperture J-factor correction are:

$$I_\gamma(E_\gamma,\psi) = \frac{k_a}{4\pi}\frac{dN_\gamma}{dE_\gamma}\int_0^{\ell_{\max}} d\ell\, n_1\Big(r(\ell,\psi)\Big)n_2\Big(r(\ell,\psi)\Big), \qquad \Delta_J(\mathcal{A}) \equiv \frac{J_{\rm NL}(\mathcal{A})}{J_{\rm local}(\mathcal{A})} - 1.$$

The directional ratio $R(\psi) \equiv I_\gamma^{\rm NL}(\psi)/I_\gamma^{\rm local}(\psi)$ and $\Delta_J(\mathcal{A})$ satisfy the exact intensity-weighted identity:

$$1 + \Delta_J(\mathcal{A}) = \frac{\int_{\mathcal{A}} I_\gamma^{\rm local}(\psi)\, R(\psi)\, d\Omega}{\int_{\mathcal{A}} I_\gamma^{\rm local}(\psi)\, d\Omega}, \qquad d\Omega = \cos b\, db\, dl = 2\pi\sin\psi\, d\psi.$$

2. Angular Redistribution vs. Net Flux Suppression

Scanning the 6×6 parameter grid over dimensionless threshold $x \equiv v_{\rm th}/v_{\rm esc}(8\ \text{kpc}) \in \{0.55, 0.70, 0.85, 0.91, 1.05, 1.20\}$ and normalized relaxation rate $y \equiv \Gamma_{\rm chem}(8\ \text{kpc})/\Omega_r^{\rm ref} \in \{0.01, 0.1, 1, 3, 16, 100\}$ establishes a fundamental distinction between angular redistribution and uniform flux rescaling:

$$\Delta_J(4\pi)_{\rm extremum} \simeq -0.0149 \quad (-1.49\%\ \text{suppression at } (x,y) = (1.20, 1)).$$

At the separately refined benchmark $(x, y) = (0.91, 0.01)$:

$$\Delta_J(4\pi) \simeq -0.0105\ \ (-1.05\%), \qquad R(\psi) \in \Big[0.976,\ 1.458\Big]\ \text{on}\ 0.02^\circ \le \psi \le 180^\circ.$$

- **Coexistence of +45.8% Central Boost & −1.05% Net Suppression:** Eccentric halo particles excited near pericentre populate the sub-kpc core ($\psi \to 0.02^\circ$, $R = 1.458$), while depleting the intermediate-angle annulus ($1^\circ < \psi < 10^\circ$, $\Delta_J = -1.3312\%$) that carries the bulk of the solid-angle-weighted luminosity $2\pi\sin\psi\, I_\gamma^{\rm local}(\psi)$.
- **Causal Forward Transport (Not Retarded Propagation):** Photons are emitted instantaneously from the reconstructed density product $n_1(r)n_2(r)$; the morphology reflects earlier orbital phases carried to the emission point by bound halo particles, not retarded photon propagation.

3. Finite-Age Evolution & Matched Local Reference

To test sensitivity to cosmological initial conditions when relaxation is slow ($\tau_r \ll 1$), we initialize all occupied phase-space cells with uniform fraction $x_{2,0} \in \{0, 0.5\}$ and evolve along backward orbits for $t_{\rm age} = 10$ Gyr against a matched local reference $\dot{x}_{2,\rm loc} = U(r)(1 - x_{2,\rm loc})^2 - D(r)x_{2,\rm loc}^2$ ($x_{2,\rm loc}(r,0) = x_{2,0}$):

$$\Delta_J^{\rm age}(\mathcal{A}) \equiv \frac{J_{\rm orb}(\mathcal{A}, t_{\rm age}; x_{2,0})}{J_{\rm loc}(\mathcal{A}, t_{\rm age}; x_{2,0})} - 1 \quad \text{(isolates transport) vs.} \quad \Delta_J^{\rm eq}(\mathcal{A}) \equiv \frac{J_{\rm orb}(\mathcal{A}, t_{\rm age}; x_{2,0})}{J_{\rm local,eq}(\mathcal{A})} - 1.$$

Rate y ($x = 0.91$)	Initial $x_{2,0}$	Matched $100\Delta_J^{\rm age}$	Equilibrium $100\Delta_J^{\rm eq}$	Physical Memory State (10 Gyr)
$y = 0.01$ (Slow)	$x_{2,0} = 0.0$	-6.116%	-9.171%	Strong Sub-Equilibrium Suppression
$y = 0.01$ (Slow)	$x_{2,0} = 0.5$	$+4.011\%$	$+7.013\%$	**Opposite-Sign Flux Enhancement**
$y = 1.00$ (Mod.)	$x_{2,0} = 0.0$	-0.933%	-0.938%	Converged Near Stationary (-0.918%)
$y = 1.00$ (Mod.)	$x_{2,0} = 0.5$	-0.898%	-0.887%	Initial-Condition Memory Erased

Finite-Age Quadrature Verification: At $t_{\rm age} = 10$ Gyr and $y = 0.01$, doubling orbital phase resolution ($512 \to 1024$) changes $\Delta_J^{\rm age}$ by $< 9.8\times10^{-8}$; refining velocity nodes ($40^2 \to 80^2$) changes it by $< 5.3 \times 10^{-5}$; doubling the radial grid changes it by $< 4.4 \times 10^{-5}$; and doubling LOS/angular quadrature changes it by $< 9.1 \times 10^{-6}$.

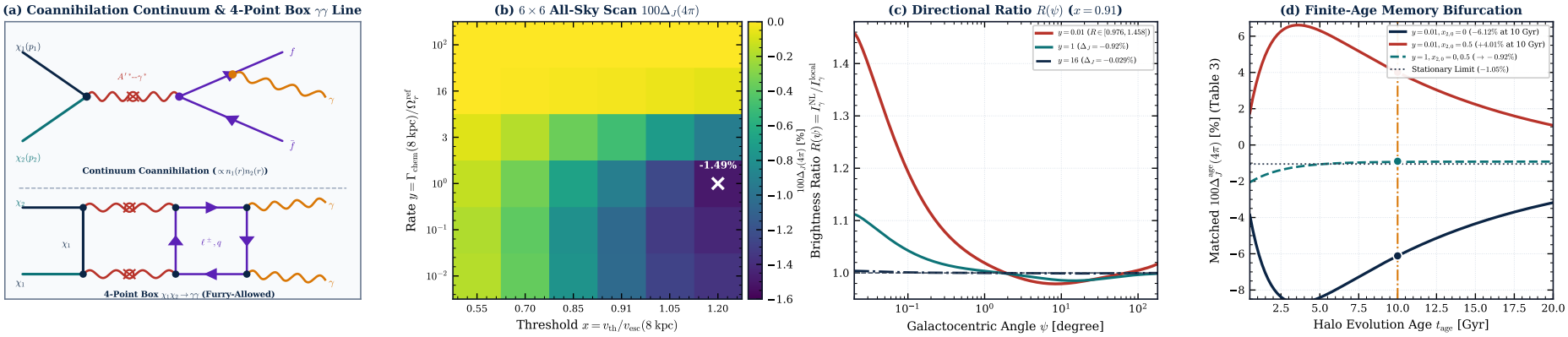


Figure 4 (Coannihilation Topologies, Nonlocal J-Factor Grid, Brightness Ratio & Finite-Age Memory): (a) Tree-level continuum coannihilation ($\chi_1\chi_2 \to A'^* \to f\bar{f}\gamma$) and Furry-allowed 4-point fermion box diagram for $\chi_1\chi_2 \to \gamma\gamma$. **(b)** Stationary 6×6 all-sky nonlocal correction $100\Delta_J(4\pi)$ showing the -1.49% extremum at $(1.2, 1)$. **(c)** Directional brightness ratio $R(\psi) = I_\gamma^{\rm NL}/I_\gamma^{\rm local}$ at $x = 0.91$ spanning $[0.976, 1.458]$ over $0.02^\circ \le \psi \le 180^\circ$. **(d)** Finite-age evolution $100\Delta_J^{\rm age}(4\pi)$ demonstrating the -6.12% vs. $+4.01\%$ initial-condition bifurcation at $y = 0.01, t_{\rm age} = 10$ Gyr.

XXXVIII IWHEPFT Synthesis: A 1.05% integrated all-sky suppression coexists with a +45.8% inner-cusp brightness boost, while slow relaxation retains an $\mathcal{O}(10\%)$ sign-reversing dependence on primordial state fractions after 10 Gyr.

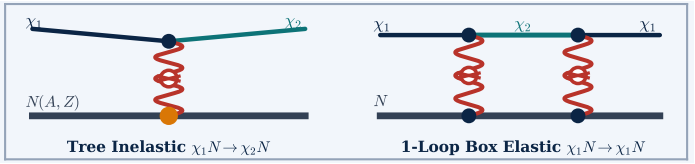
Osipkov–Merritt Anisotropy, Alternative Halo Profiles, PSF Morphology Ratio $\mathcal{R}_{\rm morph}$ & Quadrature Audit

Shide Feng and Jingxu Wu*
Faculty of Physics, Lomonosov Moscow State University
Moscow 119991, Russia • wuxj@my.msu.ru

1. Halo Profiles & Osipkov–Merritt Anisotropy Extension

Spherical symmetry alone does not imply velocity isotropy. We extend the isotropic NFW reconstruction to alternative halo profiles (Einasto $\ln[\rho(r)/\rho_{-2}] = -\frac{2}{\alpha_E}[(r/r_{-2})^{\alpha_E} - 1]$ and cored Burkert $\rho(r) = \frac{\rho_B r_B^3}{(r+r_B)(r^2+r_B^2)}$) and radial velocity anisotropy via the Osipkov–Merritt integral $Q \equiv \mathcal{E} - \frac{L^2}{2r_a^2}$:

$$\beta(r) \equiv 1 - \frac{\sigma_t^2}{2\sigma_r^2} = \frac{r^2}{r^2+r_a^2}, \qquad \rho_Q(r) = \left(1+\frac{r^2}{r_a^2}\right)\rho(r), \qquad f_{\rm OM}(Q) = \frac{1}{\sqrt{8}\pi^2}\int_0^Q \frac{d\Psi}{\sqrt{Q-\Psi}}\frac{d^2\rho_Q}{d\Psi^2}.$$



- **Anisotropy Amplification:** Radial anisotropy ($r_a = 15$ kpc) weights eccentric low-L trajectories that plunge through the high-velocity bulge, raising $R_{\rm max}$ from 1.458 (isotropic NFW) to $\mathbf{R_{max} = 1.57}$.
- **Inner Slope Sensitivity:** Einasto ($\alpha_E = 0.17$) yields $R_{\rm max} \simeq 1.34$, whereas a flat Burkert core ($r_B = 6$ kpc) reduces the radial equilibrium gradient $dx_{2,\rm eq}/dr$ and suppresses memory to $R_{\rm max} \simeq 1.06$.

2. Instrumental PSF & dSphobic Target Dichotomy

To compare angular redistribution against gamma-ray data without relying on unknown absolute flux normalizations, we define the central-to-annular morphology ratio convolved with instrument PSF $G_{\rm PSF}(\sigma_{\rm PSF})$:

$$\mathcal{R}_{\rm morph}(\sigma_{\rm PSF}) \equiv \frac{\int_{\mathcal{A}_{\rm in}} I_{\gamma,\rm PSF}(\psi)\,d\Omega}{\int_{\mathcal{A}_{\rm out}} I_{\gamma,\rm PSF}(\psi)\,d\Omega}, \qquad \begin{matrix}\mathcal{A}_{\rm in}: 0.02^\circ \le \psi \le 1^\circ \ \text{(Central Cusp)},\\ \mathcal{A}_{\rm out}: 1^\circ < \psi \le 10^\circ \ \text{(Depleted Annulus)}.\end{matrix}$$

For a heavy mediator ($m_{A'} \propto m_1$), the characteristic chemical rate scales parametrically as:

$$\Gamma_{\rm chem}(r) \sim \frac{\rho(r)}{m_1}\langle\sigma v\rangle \propto \frac{\rho(r)\,\alpha_D^2}{m_1^3} \quad \left(\text{at fixed } v_{\rm th}/v_{\rm esc} \text{ and } m_{A'}/m_1\right).$$

- **Milky Way vs. dSphobic Satellites:** In cold dwarf spheroidals ($v_{\rm esc} \sim 20$–45 km s^{-1}), $2v_{\rm esc} \ll v_{\rm th} \sim 500$ km s^{-1}, quenching local pair excitation ($\chi_1\chi_1 \to \chi_2\chi_2$) and evading joint Fermi-LAT / HAWC / H.E.S.S. / MAGIC / VERITAS dSph limits while preserving a bright Galactic Center signal.
- **Scope & Full Boltzmann Outlook:** Extending the fixed-bath radial closure to a complete particle forecast requires the velocity-changing collision operator, recoil evolution of $(\mathcal{E}, L)$, and satellite tidal stripping.

3. End-to-End Numerical Verification & Quadrature Audit

All algebraic traces, Eddington inversions, periodic segment maps, and line-of-sight quadratures are independently verified in Appendix A–C (with hyperbolic-sine splitting around the ray point of closest approach):

Numerical Verification Test (Appendix A–C)	Max Error / Change	Independent Check Method
Spinor Sum vs. Reduced Traces $T_{tt,uu,tu}$ (500 pts)	6.64×10^{-15}	Direct 4-Component Spinor Sum
Analytic $J_{0,1,2}, K_0$ vs. 160-Node Gauss–Legendre	1.00×10^{-15}	60-Digit Precision ($B/A \ll 1$)
Relativistic Cross Section Quadrature ($v_{\rm rel} \le 1.2$)	1.45×10^{-14}	Direct Angular Integration
Eddington Density Recovery (20×20 Velocity Grid)	7.20×10^{-3}	Unrenormalized $\rho(r)$ Quadrature
Eddington Density Recovery (40×40 Standard Grid)	2.39×10^{-6}	Unrenormalized $\rho(r)$ Quadrature
Eddington Density Recovery (80×80 Refined Grid)	1.31×10^{-7}	2800 Energies / 160 Abel Nodes
All-Sky Δ_J Velocity Refinement ($40^2 \to 80^2$)	4.74×10^{-6}	Local (u, μ) Orbit Quadrature
All-Sky Δ_J Phase/Radial/Central Refinement	8.82×10^{-7}	1024 Segments / 200 Radii
All-Sky Δ_J Doubled LOS & Angular Quadrature	3.15×10^{-6}	600 LOS / 320 Aperture Nodes
Nonlinear Riccati Map vs. Continuous LSODA	7.30×10^{-8}	Periodic Shooting ($y = 0.05$–0.2)
Finite-Age Cycle Matrix vs. DOP853 (10^{-12} tol.)	2.75×10^{-8}	1024 Segments (10 Gyr Run)

References: [1] D. Tucker-Smith & N. Weiner, *PRD* 64 (2001) 043502. [2] N. Arkani-Hamed et al., *PRD* 79 (2009) 015014. [3] A. Berlin et al., *JCAP* 04 (2026) 017. [4] T. R. Slatyer, *JCAP* 02 (2010) 028. [5] T. Lacroix et al., *JCAP* 09 (2018) 040. [6] S. Abdollahi et al., *JCAP* 03 (2026) 035.

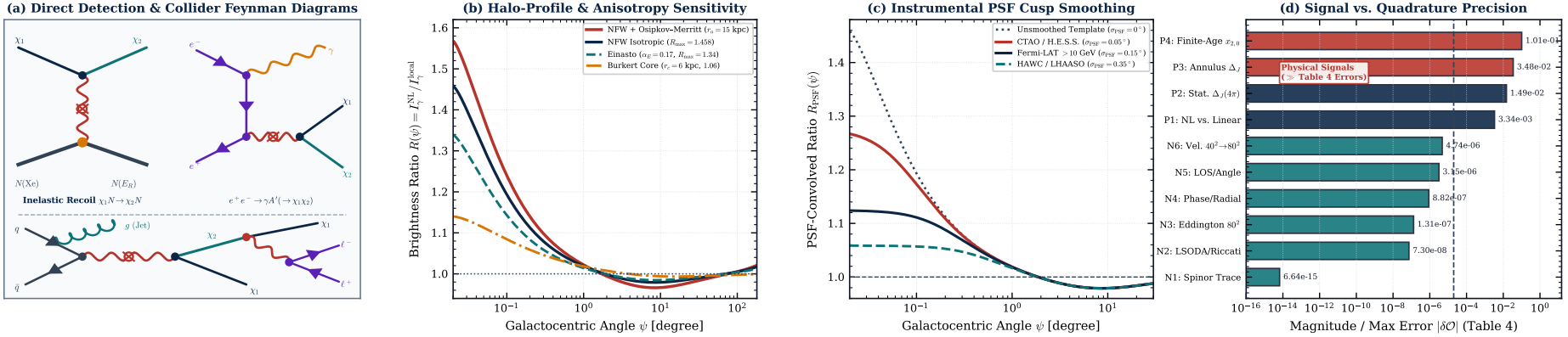


Figure 5 (Direct Detection/Collider Topologies, Halo/Anisotropy Sensitivity, PSF Smoothing & Quadrature Audit): (a) Strict-QFT Feynman diagrams for inelastic nuclear recoil $\chi_1 N \to \chi_2 N$, $e^+e^- \to \gamma A'(\to \chi_1\chi_2)$ mono-photon production, and LHC mono-jet + displaced lepton vertex. **(b)** Sensitivity of $R(\psi)$ to Osipkov–Merritt radial anisotropy ($r_a = 15$ kpc) and Einasto/Burkert density profiles. **(c)** Instrumental PSF convolution $R_{\rm PSF}(\psi)$ for CTAO/H.E.S.S. (0.05°), Fermi-LAT (0.15°), and HAWC/LHAASO (0.35°). **(d)** Comparison of physical nonlocal effects (10^{-2}–10^{-1}) against Table 4 numerical errors (10^{-15}–10^{-6}).

XXXVIII IWHEPFT Synthesis: All physical orbital-memory corrections ($\Delta_J \sim 10^{-2}$–10^{-1}) exceed numerical quadrature errors ($\lesssim 5 \times 10^{-6}$) by more than three orders of magnitude across every tested grid refinement. **Shide Feng & Jingxu Wu (MSU) • Panel 5 / 5**